Electronic Supplementary Material (ESI) for Energy & Environmental Science.

Supporting information

Nanostructure of solid electrolyte interphases and its consequences for microsized Sn anodes in sodium ion battery

Jiaqiang Huang,[a,#] Xuyun Guo,[a,#] Xiaoqiong Du,[a] Xiuyi Lin,[a] Jian-Qiu Huang,[a] Hong Tan,[a,b] Ye Zhu[a,]* and Biao Zhang[a,b,]*

[a]*Department of Applied Physics, The Hong Kong Polytechnic University, Hung Hom, Hong Kong, P.R. China*

[b]*The Hong Kong Polytechnic University Shenzhen Research Institute, Shenzhen, P.R. China*

[#]: These authors contribute equally to this work.

*Email: Dr. Biao Zhang: biao.ap.zhang@polyu.edu.hk; Dr. Ye Zhu: ye.ap.zhu@polyu.edu.hk

This file contains

Experimental and theoretical sections

Fig. S1-S27 and discussions

Including the size of Sn particles (pristine, cycled electrodes in diglyme and EC/DMC); the influence of mass loading on electrochemical performance; the cyclic stability in $NaPF_6$-based electrolytes and NVP-Sn full cell; the homolysis of diglyme, DMC and EC; the electrochemical performance using other salts ($NaClO_4$, $NaSO_3CF_3$, and NaTFSI); proposed reactions pathways of electrolyte decompositions; possible role of CMC; LUMO and HOMO of the solvents; the nanostructure of SEIs using $NaBF_4$/diglyme after 20 cycles; the nanostructure of SEIs using $NaPF_6$ as the salt; Electrodeposited Sn: morphology, crystallinity, electrochemical performance, and cryo-HAADF-STEM, TEM, and EELS mapping of the cycled electrodes; the in-depth XPS and Raman spectra of cycled electrodeposited Sn electrodes, and atomic ratios and Sn $3d_{2/3}$ spectra of the cycled Sn microparticle electrodes; derivation details of force spectroscopy; determinations of pull-off forces; histograms of Young's modulus, relative elastic region and SEI thickness; derivation details of strain of SEI upon the volume expansion; SEI strain as a function of x in Na_xSn, space utilization ratio and the void space; discussions on EIS spectra and the equivalent circuit; GITT results.

Movies 1 and 2 depict the stability of EC/DMC-derived SEI against the electron beam without and with cryo.

References

Experimental and theoretical sections

Preparations of Sn microparticle electrode

Sn (Sigma, ~10 μm, 99%) was mixed with Super P, carbon fibers, and carboxymethylcellulose sodium (Sigma-Aldrich, average Mw ~700,000) in a ratio of 7:1:1:1 by ball-milling for 1 hour in an argon atmosphere at a speed of 360 r min^{-1}. The tap density of the as-milled powder is measured as 1.3 mg cm^{-3}. The as-prepared powder was further stirred in de-ionized water and then coated on copper foil to make the electrode tap (Fig. S1a-c). $Na_3V_2(PO_4)_3$ (NVP) were casted on Al foil in a mass ratio of NVP:Super P:polyvinylidene difluoride=92:4:4. The tap was punched into electrodes with a diameter of 12 mm, which were dried under vacuum at 80 ^{o}C before the assembly of coin cells. The typical loading of the Sn electrode is ~1.0 mg$_{Sn}$ cm^{-2}. The influences of loading on the electrochemical performance in diglyme electrolyte are shown in Fig. S2.

Preparations of pure Sn microparticle electrode by electrodeposition

The electrodeposition of Sn microparticle thin film was carried out by a modified cathodic pulse method from the literature.[S1] All electrochemical depositions were carried out by a VMP system (Biologic S.A., Claix, France) at room temperature (∼22 °C) in a custom-designed three-electrode electrochemical cell, in which a rectangular copper foil at the size of ca. 35×27 mm^2 is exposed as working electrode for electrodeposition, while the rectangular pure Sn plate and an Ag/AgCl (3M KCl) electrode serve as the counter and reference electrodes, respectively. The electrodeposition bath was 45 mL of freshly prepared aqueous solution containing the 30g L^{-1} $SnCl_2$ (International Laboratory, purity 99+%) in the presence of 200g L^{-1} H_2SO_4 (Uni-Chem, 98%) as the supporting electrolyte. The deposition parameters were used as follows: pulse frequency, f=10 Hz; current density, I_s=80 mA cm^{-2}; pulse width, t_s=0.01 s; number of cycles, N=4000.

Electrochemical tests

Electrolytes were prepared by dissolving the salts [$NaBF_4$ (Alfa Aesar, purity 97%)/$NaPF_6$ (Stella Chemifa, purity >99%, water <50 ppm)/$NaClO_4$ (Dodochem, purity 99.8%)/$NaSO_3CF_3$ (Dodochem, purity 99.8%)/NaTFSI (Dodochem, purity 99.8%)] into the solvents [EC (Dodochem, purity 99.95%, water <20 ppm)/DMC (Dodochem, purity 99.95%, water <20 ppm) or diglyme (Sigma-Aldrich, anhydrous, 99.5%)] at a concentration of 1 M. Note that the electrochemical behavior in $NaPF_6$-based electrolyte is highly salt-purity-sensitive particularly for anode materials, as reported by Komaba.[S2] In contrast, the relatively low purity of $NaBF_4$ leads to a white-turbid solution as $NaPF_6$ but a stable electrochemical performance is present.

The coin cells were assembled in an argon-filled glovebox with sodium metal as the reference/counter electrode, glass fiber (Whatman, GF/D) and polypropylene (Celgard) membranes as the separators. 65 μL of electrolytes were used for each coin cell. The electrochemical behaviors of as-assembled coin cells were measured on LAND battery testers. Note that the theoretical capacity of Sn in sodium ion batteries is 1 C = 847 mAh g^{-1} based on $Na_{15}Sn_4$.

EIS results were obtained using a VMP system (Biologic S.A., Claix, France). The EIS spectra were collected at the de-sodiation state, namely after the electrodes were charged to 1 V vs.

Na^+/Na. Three-electrode configuration was adopted to exclude the influence of SEIs on the sodium counter electrode. A Swagelok-type, T-shaped cell was used with two pieces of sodium metals that individually functioned as reference and counter electrodes.

The GITT results were acquired on Arbin battery testers. The discharge/charge and rest time is 30 min. The fitting model comes from the reference,[35] which gives rise to an apparent ion diffusivity across the interfaces and inside the electrodes. The diffusivity difference may mainly ascribe to the diffusivity through SEIs because the diffusivity inside the electrode should be alike in either electrolyte.

Characterizations

We mainly studied the samples at the de-sodiated state, which are supposed to be less reactive and can benefit the TEM observations. We cycled the batteries for three cycles to construct the SEIs when the Coulombic efficiencies in diglyme electrolyte are stable and >=~99% afterwards. It indicates the negligible formation of new SEIs. Due to the continuously low Coulombic efficiencies in EC/DMC electrolyte, the same cycle number (three) was applied as a control. The electrodes for the *ex situ* characterizations were obtained by disassembling the batteries in the glove box and washing them with DMC or diglyme. Subsequently, the active materials were carefully scratched from the current collectors and transferred into the glass bottles that were filled with the corresponding solvents (diglyme or DMC). They were then shaken by hands to minimize the damage of SEIs until the liquid became slightly turbid. The resultant supernatant was then dropped onto the TEM grids for a few times. The TEM grids were evacuated and dried in the antechamber for a few hours. The whole process was done in an Ar-filled glove box. As for SEM (Tescan VEGA3), XPS, and Raman, the electrodes were directly used without dispersion.

Cryo TEM, STEM, and EELS. All TEM and STEM were performed using JEOL JEM-2100F TEM/STEM (Tokyo, Japan) operated at 200 kV, which is equipped with a Gatan Enfina electron spectrometer (CA, USA). Spectrum imaging of EELS was carried out under 200 kV accelerating voltage with a 13 mrad convergence angle for the optimal probe condition. Energy dispersion of 0.7 eV per channel and 21 mrad collection angle were set up for EELS, HAADF images were acquired with an 89 mrad inner angle simultaneously. The Sn, O, C, Na, and F intensity maps were extracted from the EELS spectrum image by integrating across the energy windows of 550-562 (M4,5 edge), 530-544 (K edge), 283-308 (K edge), 1071-1108 (K edge), and 683-785 (K edge) eV, respectively. 0.3 eV per channel energy dispersion was selected for high energy resolution C-K edge EELS analysis. The samples were firstly fabricated on TEM grids as mentioned above and then transferred to a double tilt nitrogen cooling holder, locked by a beryllium hexring (Gatan, model 636). All sample preparation and holder assembling processes were operated under inert Ar atmosphere in a glovebox. Before taking out the holder into the ambient air, the holder tip was sealed by a plastic cap and then wrapped by a Parafilm tape. Once the sealed holder was taken out from the glovebox, it was inserted into the TEM column as quickly as possible for immediate cryo-EM study. After adding the liquid nitrogen into the Dewar, the system was stabilized for at least 40 min before observation to minimize the vibration, operated under ~-175 ^{o}C. As a control group, the sample with the same fabricating procedure was transferred to a regular double-tilt beryllium holder (JEOL) for comparison.

The two videos for illustrating the beam damage influence under cryo- and regular EM were both taken under 200 kX. The corresponding dose rate (units of number of electrons per square angström per second, $e^- Å^{-2}\cdot s^{-1}$) was recorded and calibrated, equaled to around 443 $e^- Å^{-2}\cdot s^{-1}$.

XPS. XPS (Thermo Scientific, ESCALAB 250Xi) was conducted using a monochromatic Al Kα radiation (hν = 1486.6 eV) with a spot size of 500 μm. The parameters of argon sputtering were tested to ensure the gradual increase of the metallic Sn signal in the EC/DMC-derived SEI. Finally, an ion energy of 3000 eV was selected with a high current and a raster size of 2 mm, and an etch cycle time of 25 seconds was identified as a modest time gap. The estimated sputter rate was 0.67 nm s^{-1} for Ta_2O_5. The spectra of the slurry-coated electrodes were calibrated by Na 1s at 1071.1 eV, due to the complexity of C 1s. The spectra of the electrodeposited Sn were calibrated by C 1s at 284.8 eV instead, thanks to the clean C 1s.

Raman. Raman spectra were collected by a confocal Raman microscopy (Witec, alpha 300). An excitation wavelength of 532 nm was applied. The electrodes for Raman were evacuated for hours and rested in the glove box to minimize the solvent. A Swagelok-type cell (EL-Cell) was utilized for Ar atmosphere.

AFM. The AFM was conducted on a scanning probe microscope (Asylum Research, MFP 3D Infinity) using the closed fluid cell (Asylum Research), which were assembled in the Ar-filled glovebox to ensure the inert atmosphere. N-type Si indenter (APPNANO) with a radius of ~8 nm was applied, and their spring constants (20-50 nN nm^{-1}) were determined by the thermal method. Namely, the virtual deflection of the optical path and inverse optical lever sensitivity of the cantilever were determined on a clean, quasi-infinitely hard silicon wafer. The resonant frequency of the cantilever was then determined far away from the surface. The typical loading rates include 200 or 500 nm s^{-1}. The typical trigger point is 0.5 V as the deflection voltage or 350 nN; however, it may vary to collect the pull-off forces or test the condition.

At least two different electrodes for each electrolyte were tested, in which force spectroscopies were collected from several particles. The AFM images were obtained via the tapping mode. The scan size ranged from 25×25 μm^2 to 200×200 nm^2 so as to identify the microsized Sn particles in the electrodes and minimize the noises from nanosized additives such as carbons during the force spectroscopy, see Fig. S17 as an example. In addition, the force spectroscopies of carbon SP was measured, which shows a sharply dropped force response (Fig. S19c,d). The scan rates of 1 to 0.25 Hz were used together with a resolution of 256×256 $pixel^2$. Images before and after the force spectroscopies were collected to see whether there was any sample drift due to the tip-sample interactions.

Notes for the influence of carbons and binders on SEIs and AFM. The complexity from carbon SP conductive additive could be easily excluded by region selection via tapping imaging. We utilized tapping imaging, which only induces minimal interactions between the tip and sample, to acquire the morphology of the dispersed particles. Microsized, spherical particles were then selected for more detailed textures at gradually reduced scan area, since they are less possibly an aggregate of carbons. The imaging with a scan area down to 200×200 nm^2 and 256×256 pixels provides a high resolution to discern the suspicious Super P carbons (a diameter of tens of nanometers) and carbon nanofibers (VGCF, a dimeter of ~150 nm). We then measured force spectroscopies on the regions without suspicious carbons. Binders (CMC) do not have distinguishable morphologies and cannot be excluded via imaging. Therefore, CMC may be involved in the SEIs since they may not prevent the SEI formation even when they cover the surface of Sn (Fig. S8). We believe that CMC may influence the measured mechanical properties, but it is not the determinant factor since its presence does not stabilize the electrochemical performance in EC/DMC.

On top of the above considerations, we have electrodeposited pure Sn onto the copper foil (Fig. S12a-c). This provides a feasible electrode without carbons and binders (Fig. S12d,e). Cryo-TEM (Fig. S13) and AFM (Fig. S21) were applied to the cycled electrodes, and similar trends are observed in terms of relative elastic region and Young's modulus (Fig. 4g, "+"-marked points).

The thickness of SEI was measured from the interaction point (where the force starts to increase) to the fracture point (at the local force minimum), see Fig. 4c or Fig. S18. Without the fracture point, the thickness of SEI was estimated from the interaction point to the midpoint of the transition or non-linear elastic region, see Fig. 4f. See more analysis details in the below section, force spectroscopy. The simplified methodology applied here does not carefully consider the early response of the substrate (because Sn is much stiffer than SEIs, Young's modulus: ~50 GPa), creeping behaviors (because the measurement is done within a few seconds), and interfacial bonding between SEI and substrate, etc. However, we believe the results provide correct qualitative comparisons, particularly when the distinguishable responses are shown.

Theoretical calculations

DFT calculations were conducted using projected augmented wave method[S3] implemented in the Vienna Ab initio Simulation Package[S4] with the generalized gradient approximation as parameterized by Perdew-Burke-Ernzerhof.[S5] The Van der Waals forces were approximated via the DFT-D2 method.[S6] Spin polarization was considered in all cases. The molecules or radicals were isolated in a 25 Å × 25 Å ×25 Å cell. An energy cutoff of 500 eV was applied together with a Gamma-centered 1 × 1 × 1 k-point mesh. The energy and force convergence criteria were 10^{-6} eV and 0.02 eV $Å^{-1}$, respectively.

Size of Sn particles

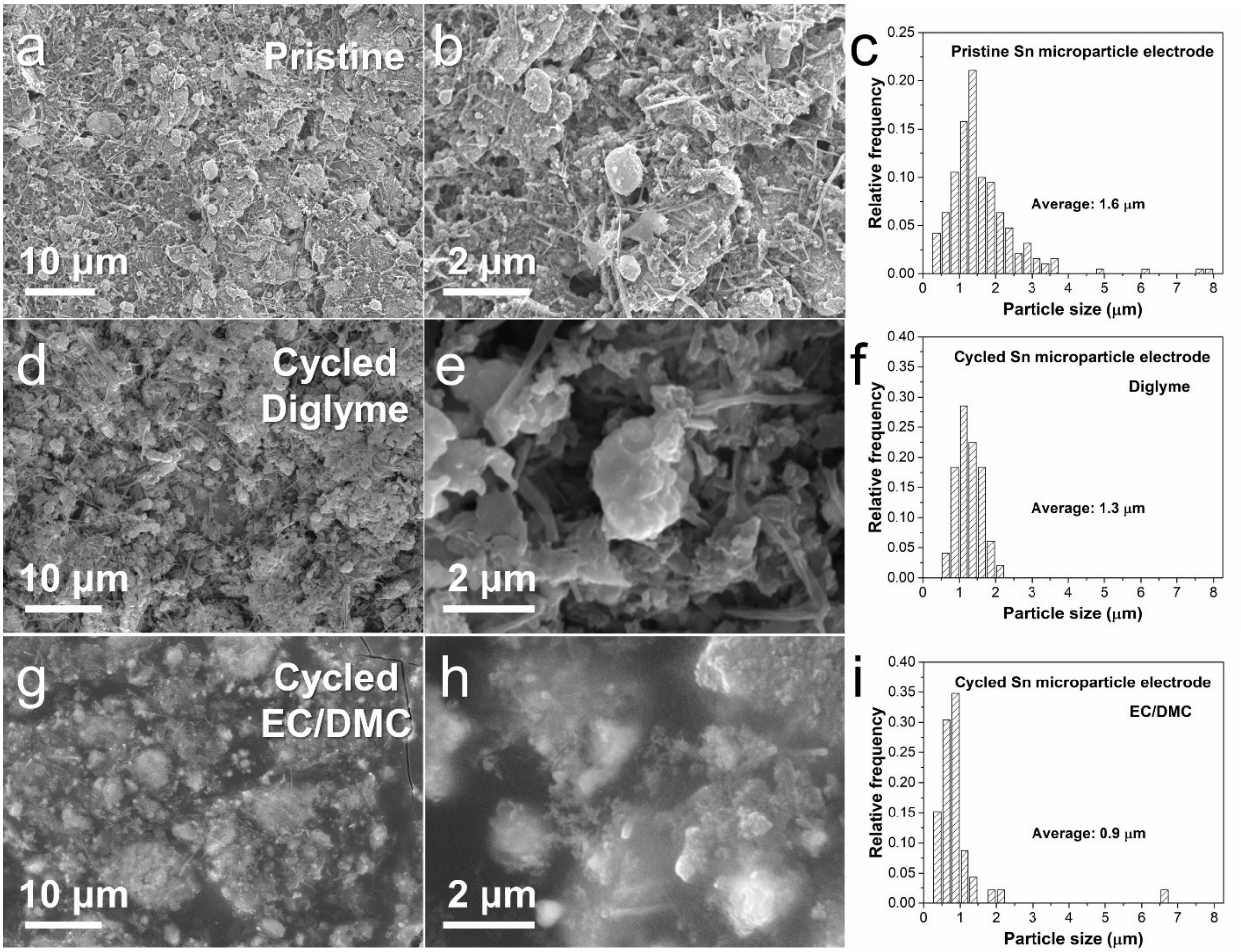

Fig. S1 SEM images and the histograms showing the size distributions of Sn particles in (a,b,c) pristine, (d,e,f) cycled electrodes using $NaBF_4$/diglyme electrolyte, and (g,h,i) cycled electrodes using $NaBF_4$/EC/DMC electrolyte.

Influence of mass loading on the electrochemical performance of $NaBF_4$/diglyme

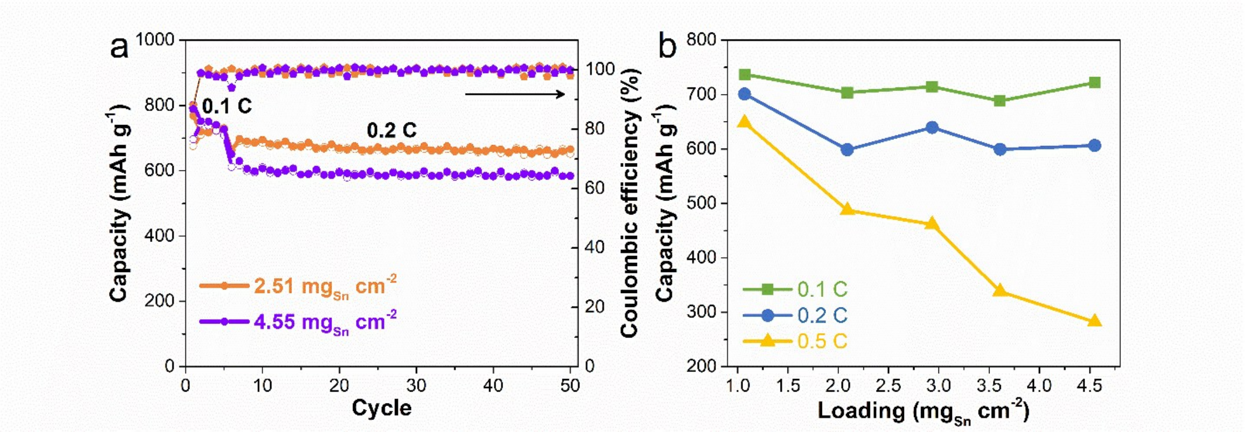

Fig. S2 The influences of mass loading on (a) capacity retention and (b) rate capability of Sn microparticle electrodes in the $NaBF_4$/diglyme electrolyte.

Cyclic stability in $NaPF_6$-based electrolytes and NVP-Sn full cell

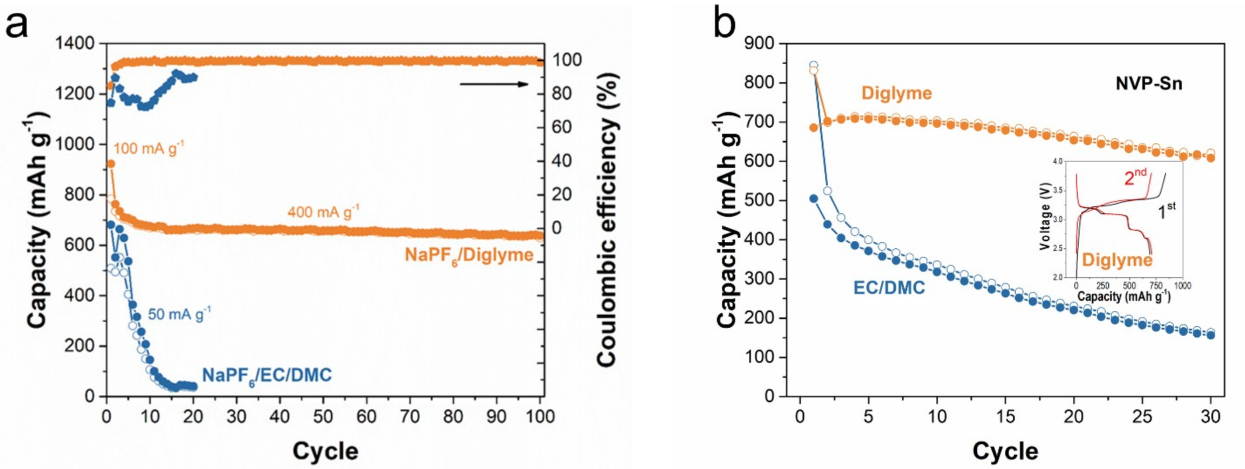

Fig. S3 (a) Cyclic stability of Sn microparticle electrodes in $NaPF_6$/diglyme and $NaPF_6$/EC/DMC electrolytes. (b) Cyclic performance of $Na_3V_2(PO_4)_3$-Sn full cell at a rate of 0.2C. Inset: electrochemical curves in diglyme. The mass ratio of NVP to Sn is ~8.

Homolysis and bond-dissociation energy

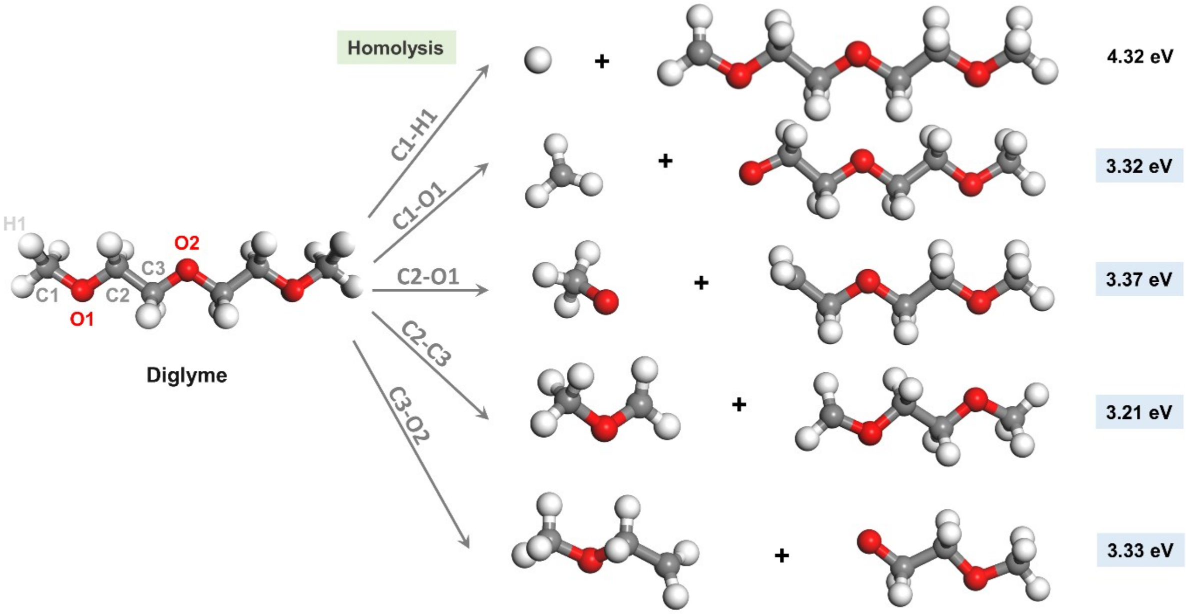

Fig. S4 The detailed homolysis of diglyme for the bond-dissociation energy calculations.

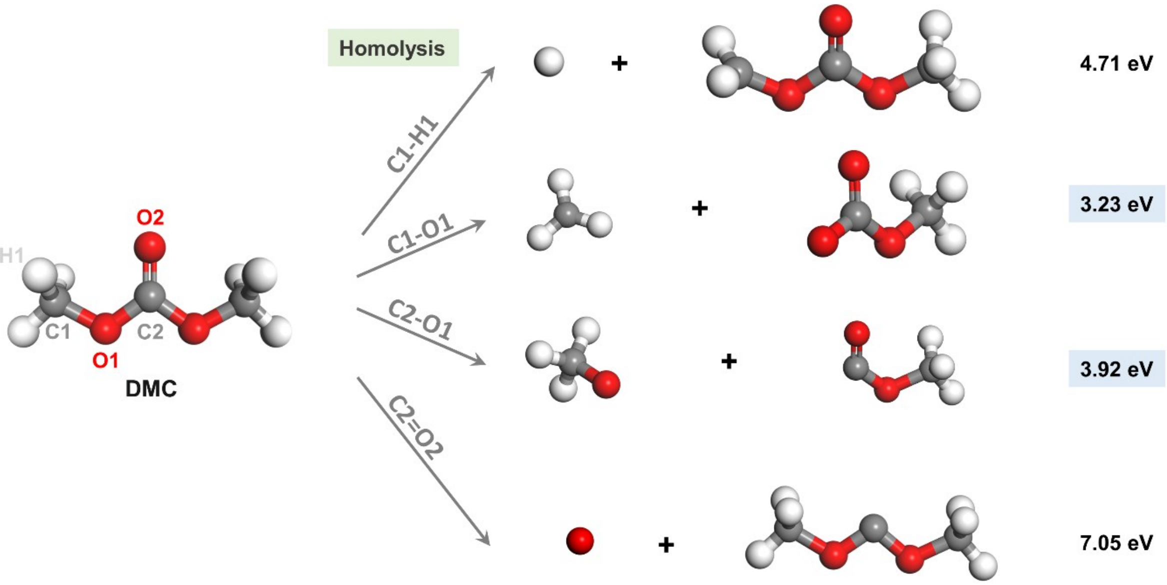

Fig. S5 The detailed homolysis of DMC for the bond-dissociation energy calculations.

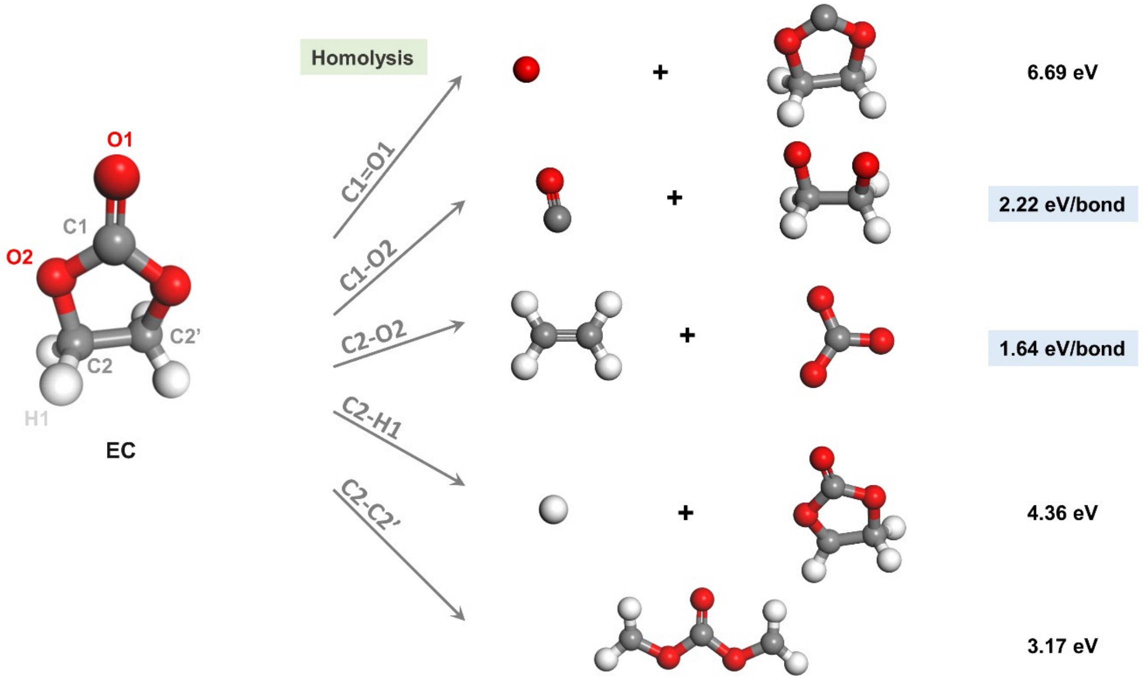

Fig. S6 The detailed homolysis of EC for the bond-dissociation energy calculations.

The electrochemical performance using other salts ($NaClO_4$, $NaSO_3CF_3$, and NaTFSI)

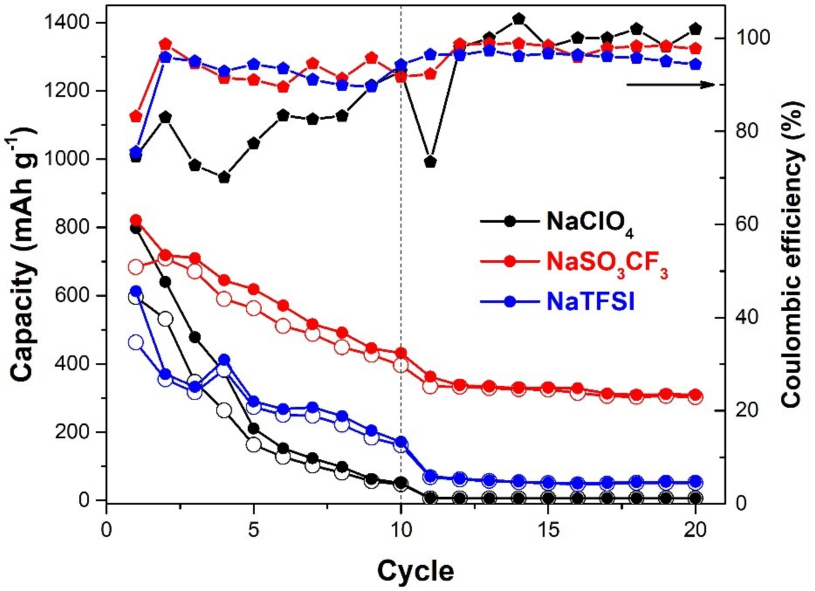

Fig. S7 The electrochemical performance of Sn microparticle electrode using $NaClO_4$, $NaSO_3CF_3$, and NaTFSI in diglyme. The first ten cycles were performed at 0.1 C, followed by 0.2 C.

Proposed reactions pathways of electrolyte decompositions

Decomposition of $NaBF_4$ or $NaPF_6$ (M = B or P),

$$NaMF_n \rightleftharpoons NaF + MF_{n-1} \tag{S1}$$

Diglyme,

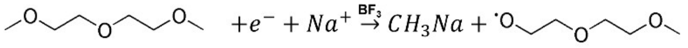

(S2)

which refers to the homolysis regarding C1-O1 in Fig. S4.

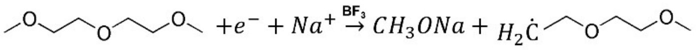

(S3)

which refers to the homolysis regarding C2-O1 in Fig. S4.

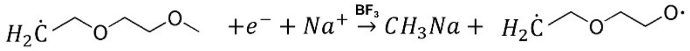

(S4)

which refers to the homolysis regarding C1-O1 in Fig. S4.

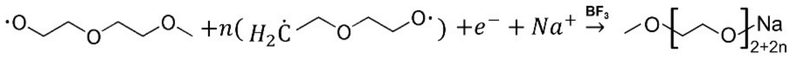

(S5)

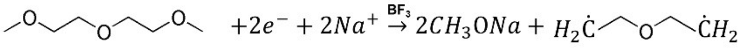

(S6)

which refers to the homolysis regarding C2-O1 in Fig. S4.

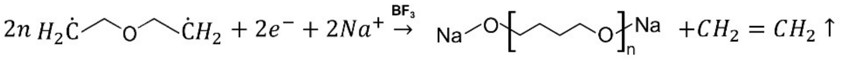

(S7)

DMC,[S7, 8]

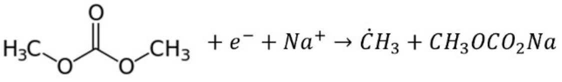

(S8)

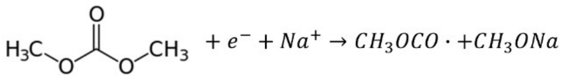

(S9)

EC,[S7, 8]

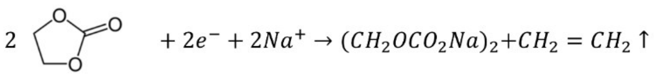

(S10)

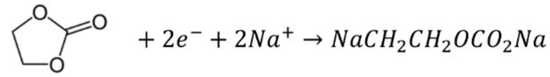

(S11)

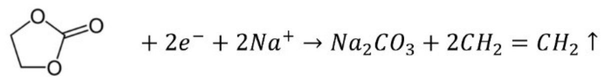

(S12)

H_2O,[S7]

$$H_2O + e^- + Na^+ \rightarrow NaOH + \frac{1}{2}H_2\uparrow \tag{S13}$$

$$NaOH + e^- + Na^+ \rightarrow Na_2O + \frac{1}{2}H_2\uparrow \tag{S14}$$

CO_2,[S7]

$$2CO_2 + 2e^- + 2Na^+ \rightarrow Na_2CO_3 + CO\uparrow \tag{S15}$$

H_2O and EC,[S7]

$$H_2O + (CH_2OCO_2Na)_2 \rightarrow Na_2CO_3 + CO_2\uparrow + (CH_2OH)_2 \tag{S16}$$

H_2O and $NaBF_4$ or $NaPF_6$ (M = B or P),

$$MF_{n-1} + H_2O \rightarrow 2HF + MF_{n-3}O \tag{S17}$$

$$MF_{n-3}O + ke^- + kNa^+ \rightarrow NaF + Na_xMOF_y \tag{S18}$$

Note that Eq. S18 do not show the exact stoichiometry, but rather the basic equations.

H_2O, $NaBF_4$ and EC,[S7, 9]

$$2HF + (CH_2OCO_2Na)_2 \rightarrow 2NaF + (CH_2OCO_2H)_2 \tag{S19}$$

H_2O, $NaBF_4$, and EC/CO_2,[S7, 9]

$$2HF + Na_2CO_3 \rightarrow 2NaF + H_2CO_3 \tag{S20}$$

H_2O, $NaBF_4$ and DMC,[S7, 9]

$$CH_3OCO_2Na + HF \rightarrow NaF + CH_3OCO_2H \tag{S21}$$

$$CH_3ONa + HF \rightarrow NaF + CH_3OH \tag{S22}$$

Possible role of CMC

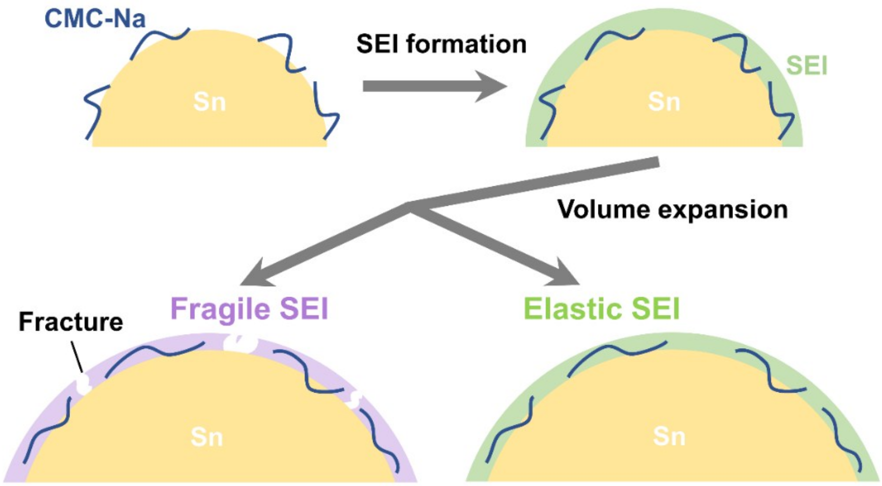

Fig. S8 A schematic showing the possible role of binders in SEIs.

LUMO and HOMO of the solvents

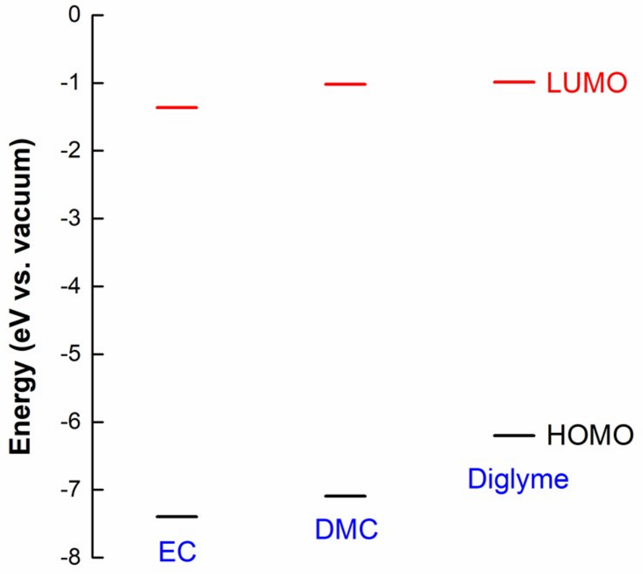

Fig. S9 The calculated LUMO and HUMO of EC, DMC and diglyme.

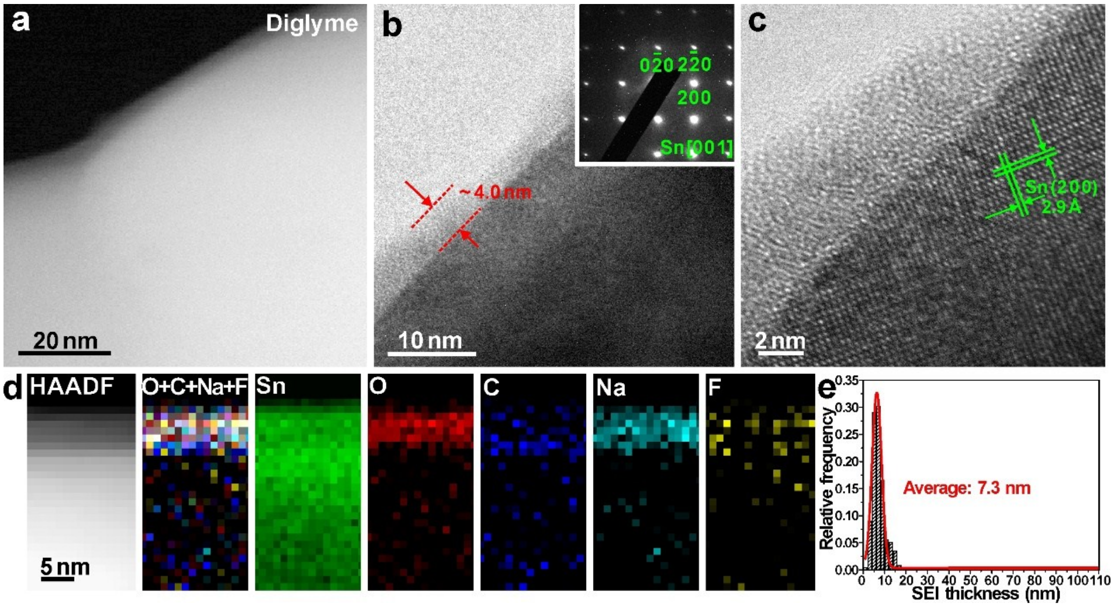

Fig. S10 Cryo HAADF-STEM (a), TEM (b,c) images and EELS mapping (d) of SEI in $NaBF_4$/diglyme after 20 cycles with SAED as inset in (b). (e) Histogram showing the distribution of SEI thickness with >250 spots.

Nanostructure of SEIs using $NaPF_6$ as the salt

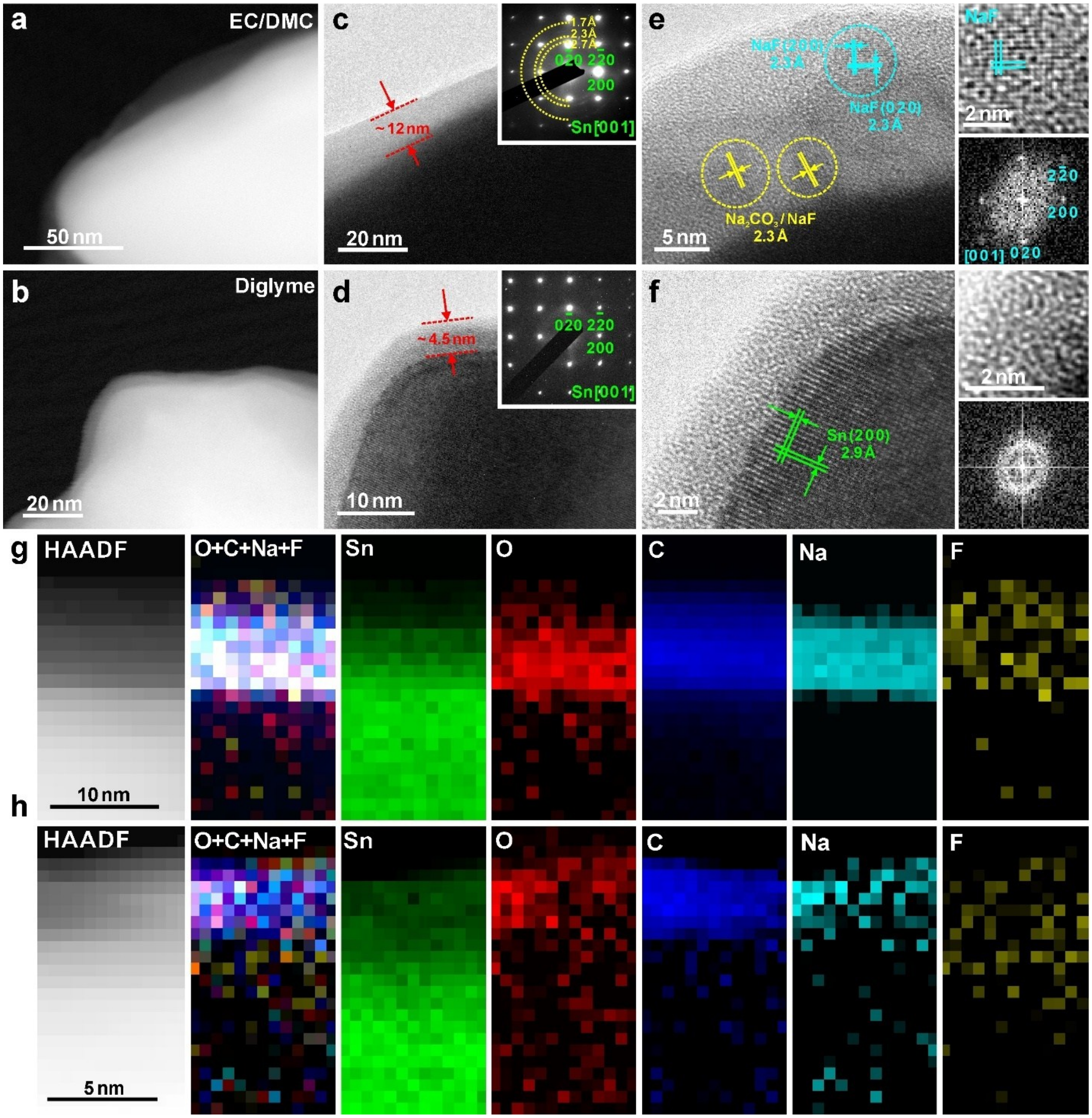

Fig. S11 HAADF-STEM, TEM images and EELS mapping of SEIs in $NaPF_6$/EC/DMC (a, c, e, and g) and $NaPF_6$/diglyme (b, d, f, and h) with SAED as insets in (c, d). Note that the insets in e and f are the enlarged HRTEM and FFT images for the SEI layer region.

Electrodeposited Sn

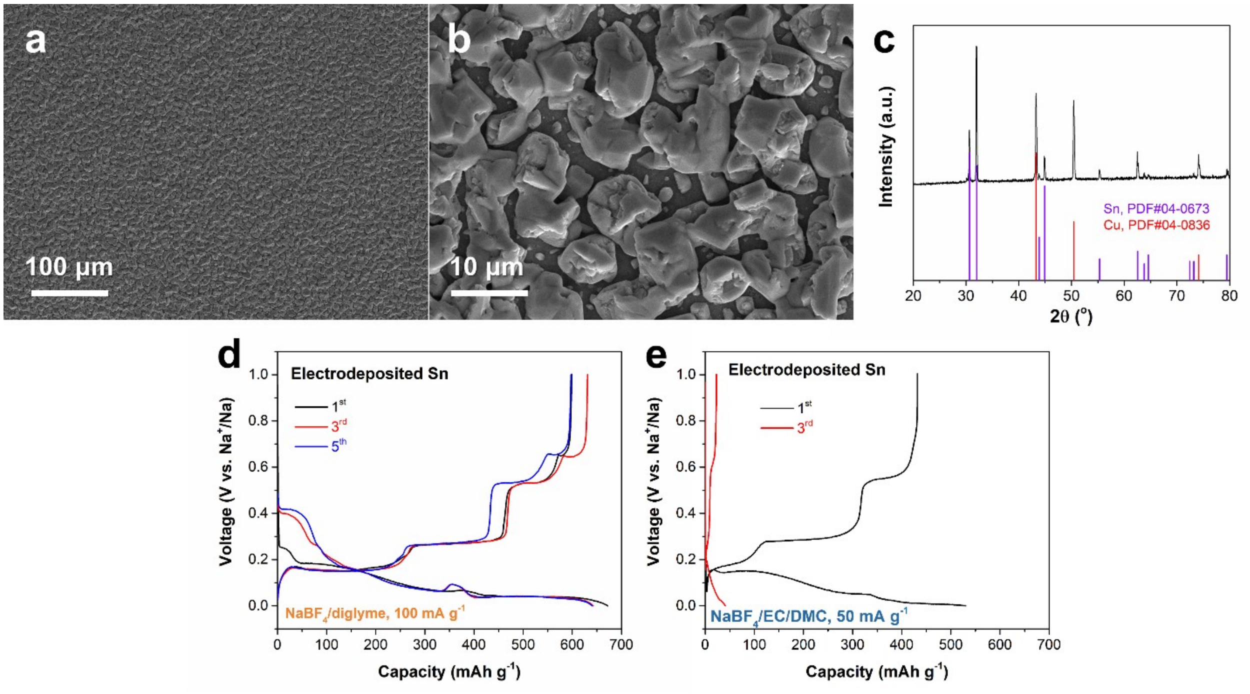

Fig. S12 (a,b) The SEM images and (c) XRD patterns of electrodeposited Sn, and (d,e) the electrochemical behaviors in $NaBF_4$/diglyme (d) and $NaBF_4$/EC/DMC (e) electrolytes.

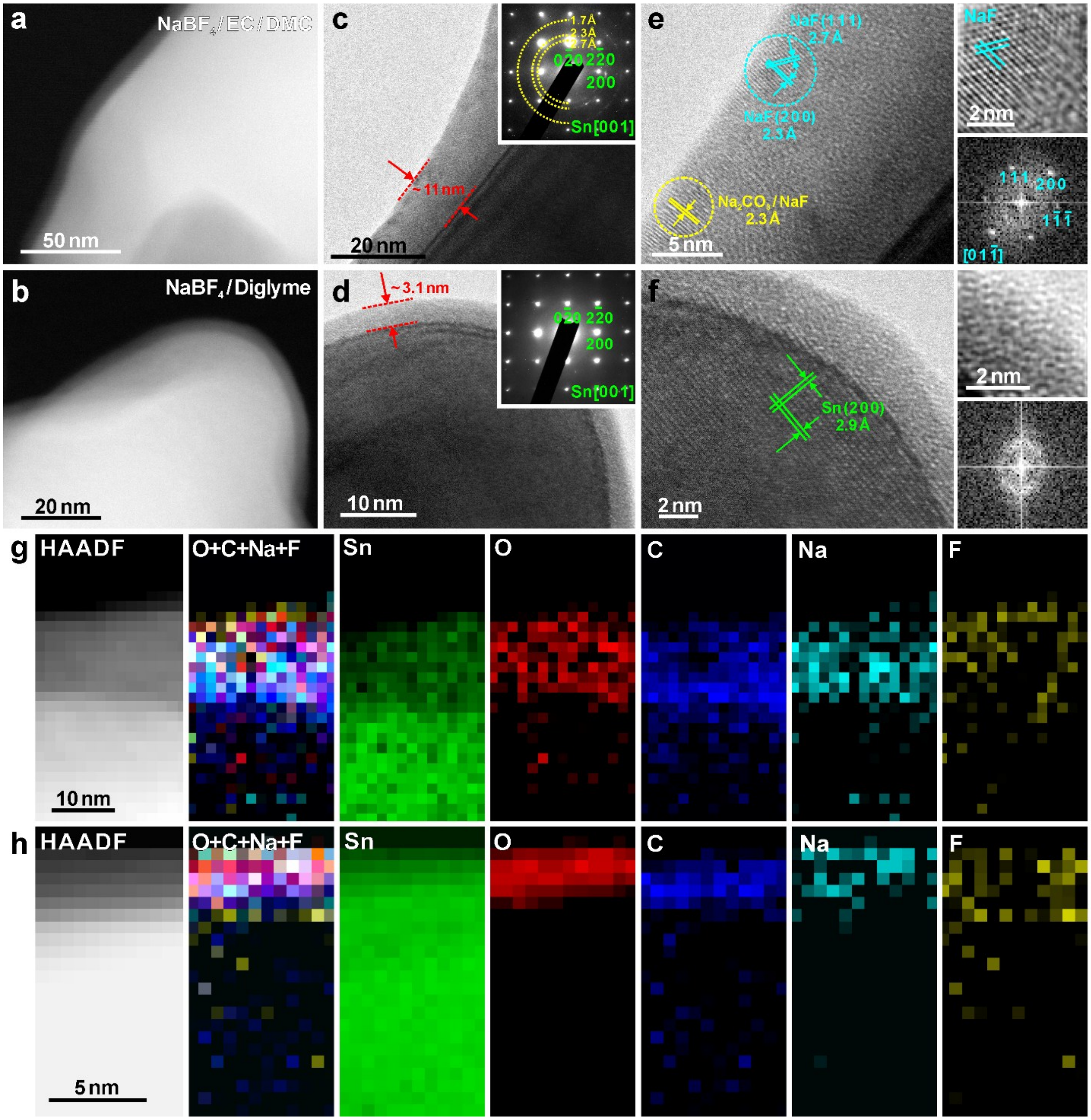

Fig. S13 Cryo HAADF-STEM, TEM images and EELS mapping of SEIs of electrodeposited Sn in $NaBF_4$/EC/DMC (a, c, e, and g) and $NaBF_4$/diglyme (b, d, f, and h) with SAED as insets in (c, d). Note that the insets in e and f are the enlarged HRTEM and FFT images for the SEI layer region.

In-depth XPS and Raman spectra

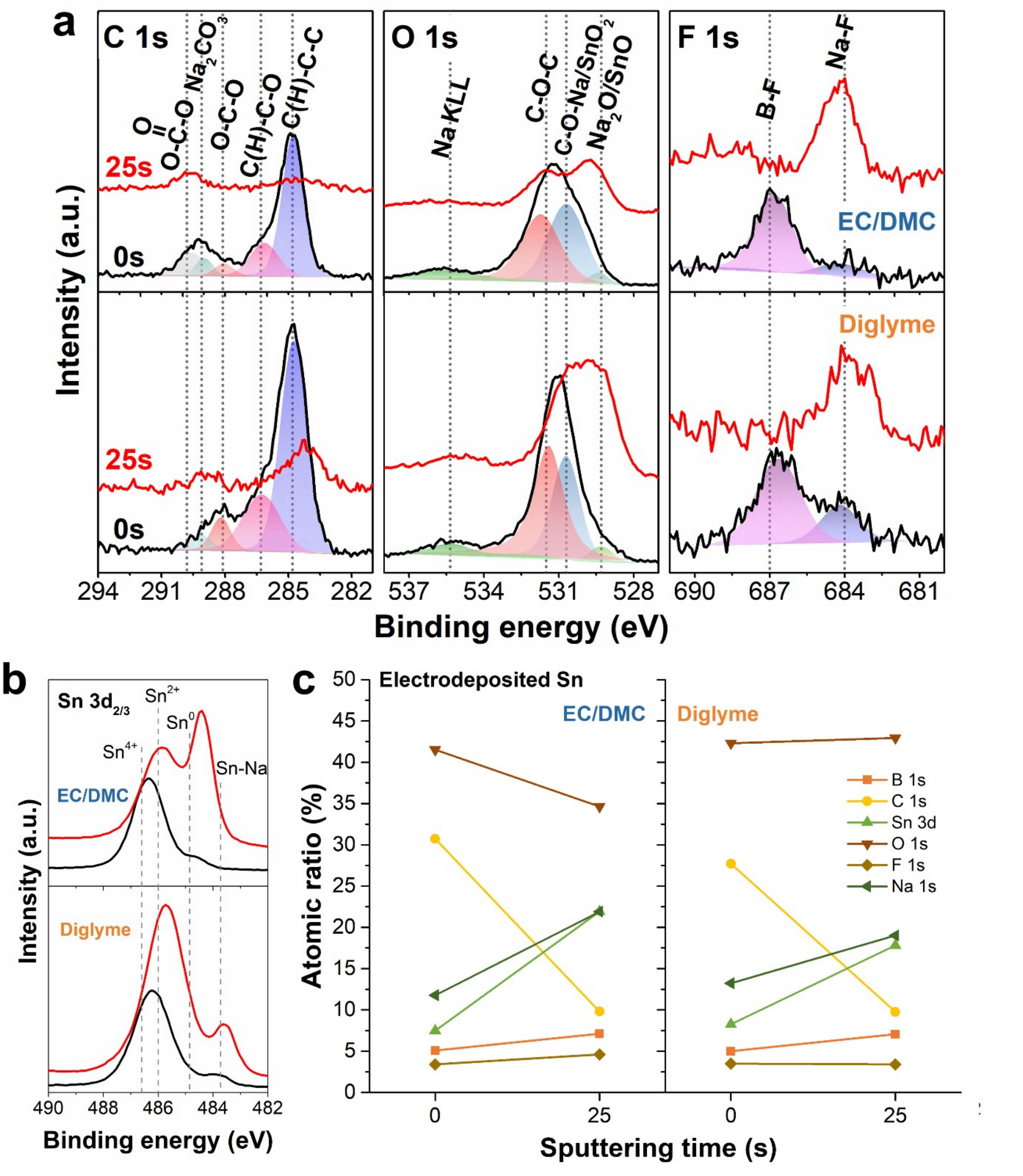

Fig. S14 (a) In-depth XPS spectra of C 1s, O 1s, F 1s, (b) Sn 3d$_{2/3}$, and (c) the corresponding atomic ratios of SEIs of electrodeposited Sn in NaBF$_4$/EC/DMC and NaBF$_4$/diglyme. Argon sputtering was applied to acquire the depth profiles.

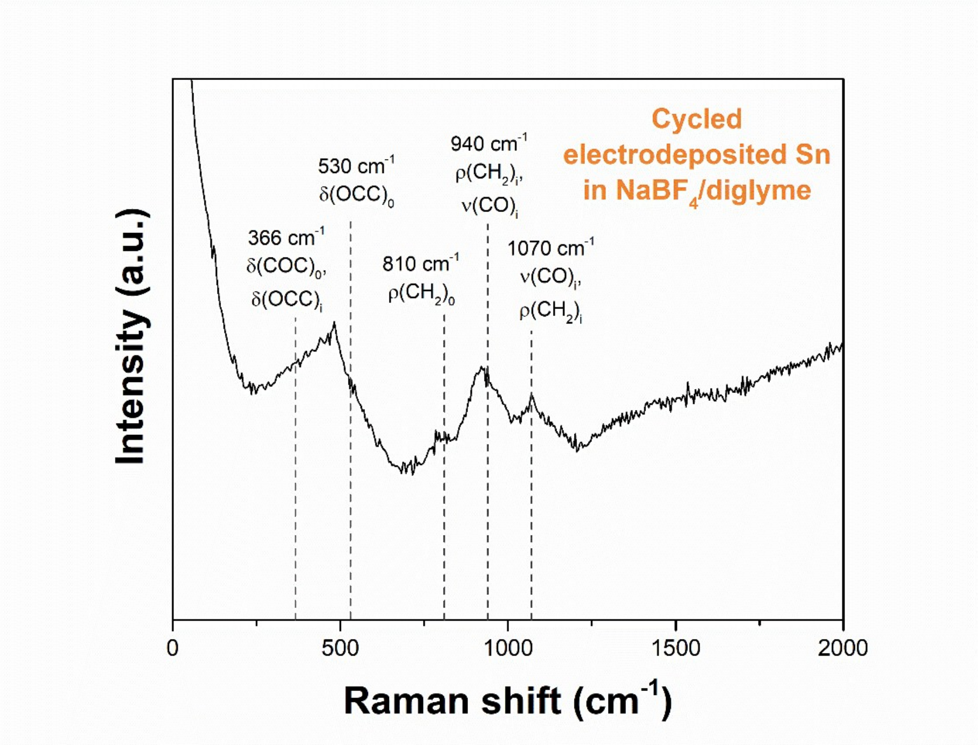

Fig. S15 Raman spectrum of electrodeposited Sn electrodes after cycles in the NaBF$_4$/diglyme electrolyte.

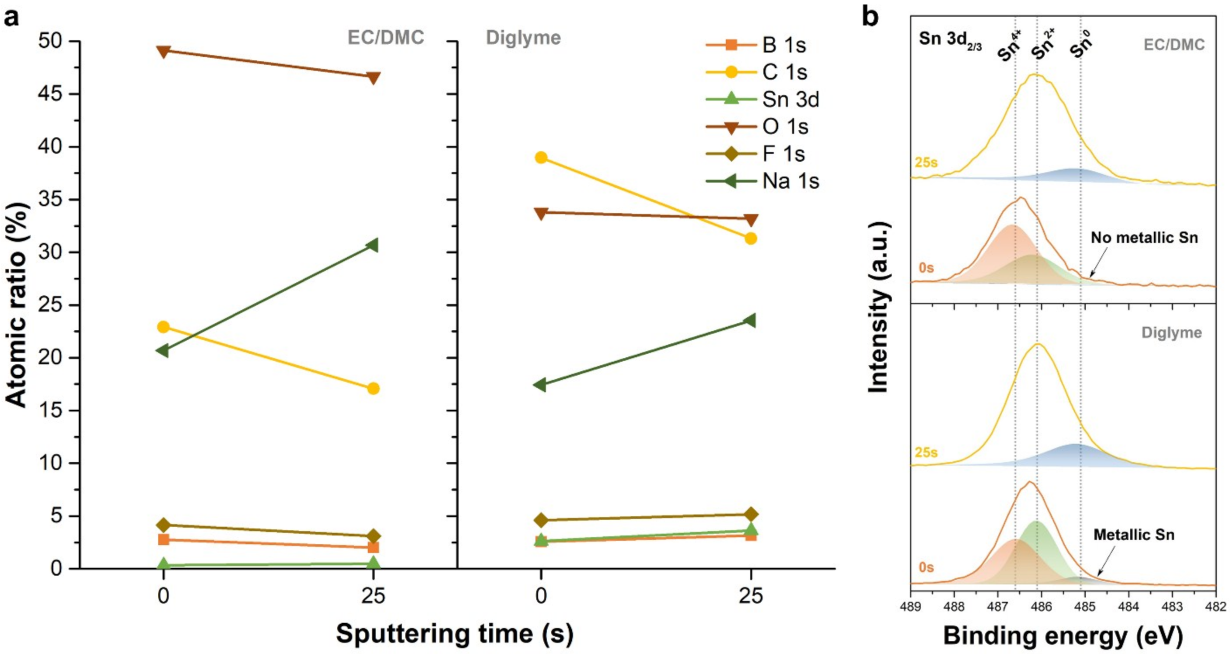

Fig. S16 (a) The atomic ratios of in-depth XPS and (b) the Sn 3d$_{2/3}$ spectra of the cycled Sn microparticle electrodes in NaBF$_4$/EC/DMC and NaBF$_4$/diglyme. The Sn 3d$_{2/3}$ spectra suggest that the metallic Sn has been detected before the argon sputtering in the diglyme sample in contrast to the case in EC/DMC.

Force spectroscopy

The derivation of equation 1 according to the DMT model was shown as follows. The model gives

$$a_{DMT}^3 = \frac{R}{K}(P - P_{c,DMT}) \tag{S23}$$

where a_{DMT} is the radius of the contact circle, R is the equivalent radius, P is the indenter load, $P_{c,DMT}$ is the pull-off force, namely, the critical force to separate the indenter and the sample, and K is the equivalent elastic modulus of the indenter and the sample, as

$$K = \frac{4}{3}\left(\frac{1 - \nu_1^2}{E_1} + \frac{1 - \nu_2^2}{E_2}\right)^{-1} \tag{S24}$$

where ν_1 and ν_2 are the Poisson's ratios of the sample and the indenter, respectively, and E_1 and E_2 are the Young's moduli of the sample and the indenter, respectively. Since the Young's modulus of Si indenter (E_2) is ~100 GPa in comparison to a few GPa or less of the SEI,[S10]

$$K \approx \frac{4E_1}{3(1 - \nu_1^2)} \tag{S25}$$

In addition,

$$R = \frac{R_1 R_2}{R_1 + R_2} \tag{S26}$$

where R_1 and R_2 are the radii of the sample and the indenter, respectively. Since the Sn microparticle electrode and its SEI have a micrometer-scale radius in comparison to the one of indenter (~8 nm),

$$R \approx R_2 \tag{S27}$$

With the assumption

$$a_{DMT}^2 = \delta R \tag{S28}$$

where δ is the indentation depth, given by

$$\delta = \Delta z - \Delta d \tag{S29}$$

where z is the z-piezo position, and d is the cantilever deflection.

The combination of equations S23, S25, S27, and S28, gives rise to equation 1.

The indenter load P is calculated as follows.

$$P = k\Delta d \tag{S30}$$

where k is the spring constant of the indenter determined by the thermal method.

The pull-off forces, $P_{c,DMT}$, were averaged from force spectroscopies using very low trigger points, see two representative curves in Fig. S19a,b.

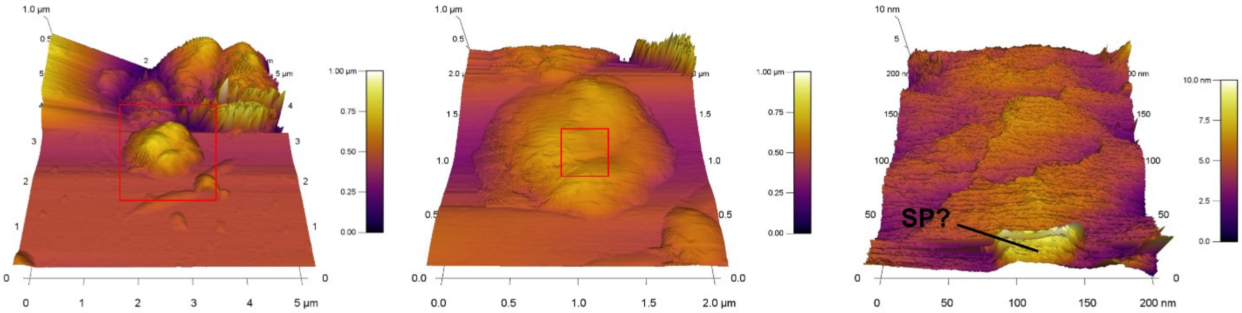

Fig. S17 The gradually enlarged AFM images of a sample spot from 5 × 5 µm^2 to 200 × 200 nm^2. The force responses from the carbon SP-like region were excluded for analysis.

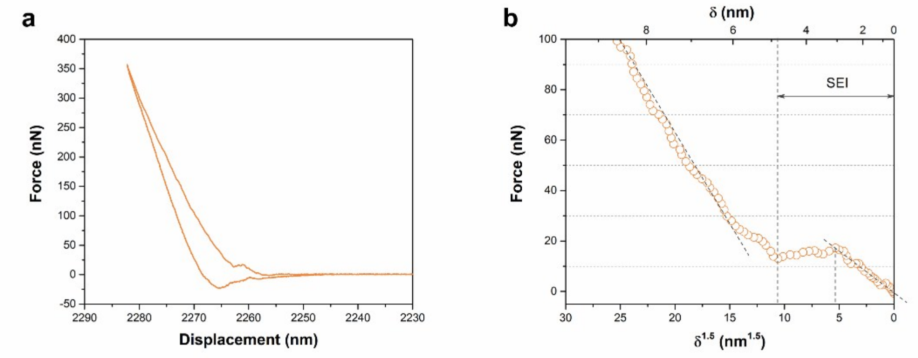

Fig. S18 Force spectroscopies of fracture behavior in diglyme-derived SEI.

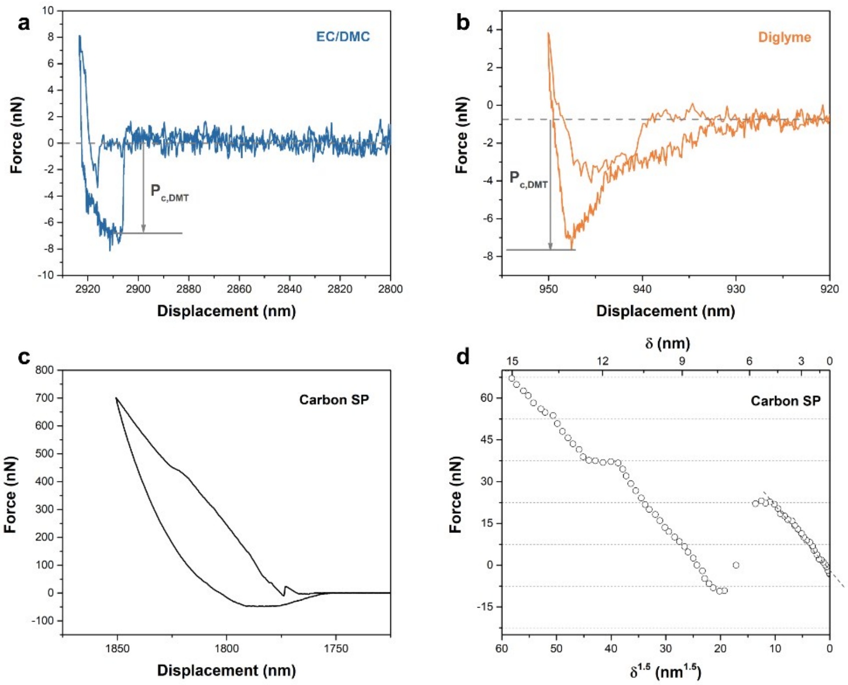

Fig. S19 (a,b)Two representative force-displacement curves for the determinations of pull-off forces. (c,d) Typical force spectroscopies of carbon SP, which shows a sharp force drop.

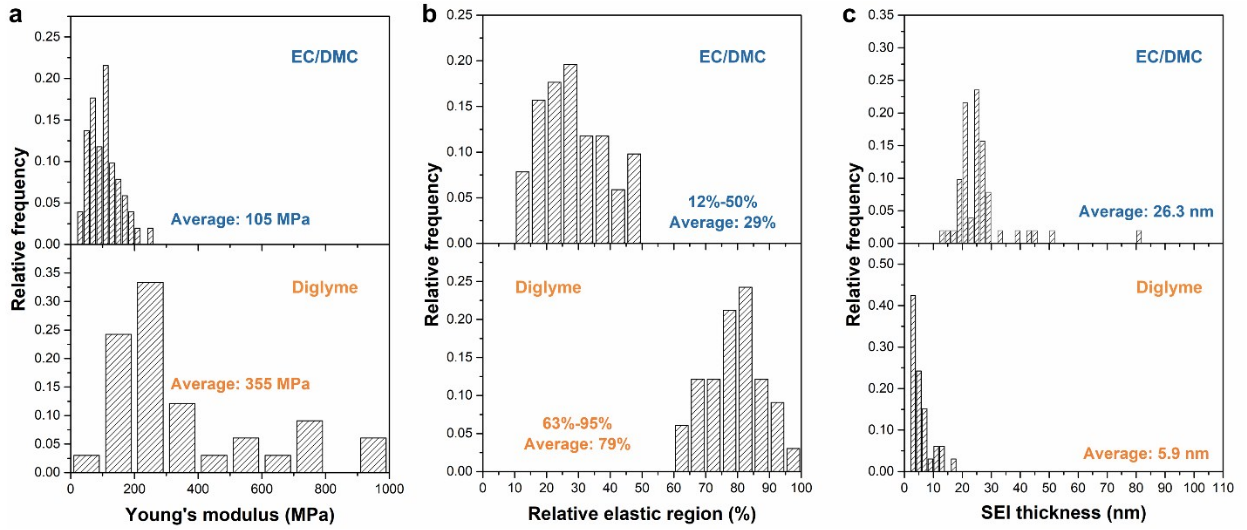

Fig. S20 Histograms of (a) Young's modulus, (b) relative elastic region, and (c) thickness of $NaBF_4$/EC/DMC- (up) and $NaBF_4$/diglyme-derived (down) SEIs.

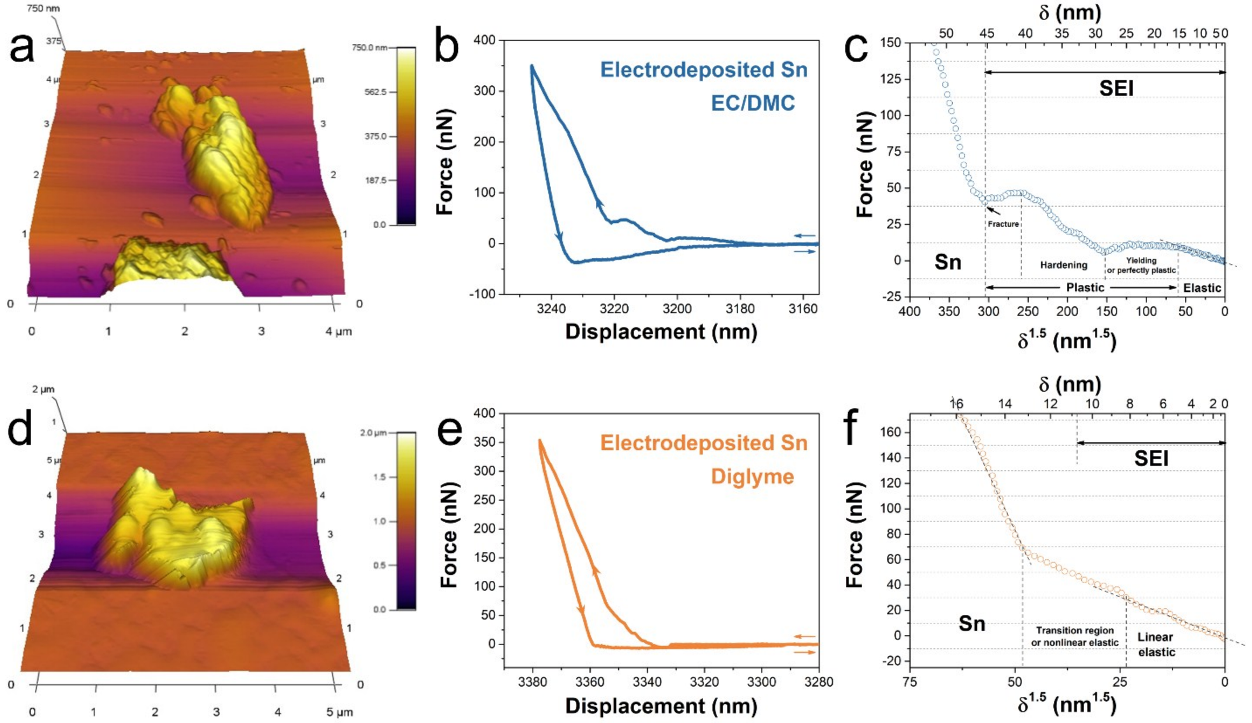

Fig. S21 (a-f) AFM images, representative force spectroscopies and their detailed analysis of SEIs of electrodeposited Sn in (a-c) $NaBF_4$/EC/DMC and (d-f) $NaBF_4$/diglyme.

The strain of SEI upon the volume expansion

To simplify the model, Sn and Na_xSn electrodes are assumed as spheres, while the SEI layers remain conformal through the whole model (Fig. S22).

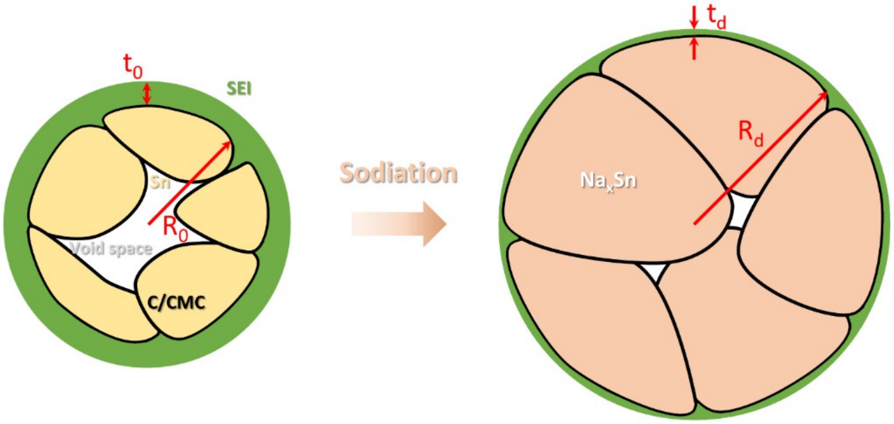

Fig. S22 A schematic illustration of the volume expansion upon the sodiation of Sn and the consequently strained SEI. Note that the black lines denote carbons and CMC.

The radii of Sn and Na_xSn electrode spheres are R_0 and R_d, respectively. The thicknesses of the SEI before and after the volume expansion are t_0 and t_d, respectively. The gravimetric void space of the electrode is defined as φ in $cm^3\ g^{-1}$. To estimate the strain on SEI, the volume of SEI is assumed as a constant. Before the volume expansion,

$$\frac{4}{3}\pi R_0^3 = V_{void,0} + V_{electrode,0} = m_{electrode,0}\varphi + V_{electrode,0} \tag{S31}$$

$$V_{electrode,0} = V_{Sn} + V_{C/CMC} = \frac{m_{Sn}}{\rho_{Sn}} + \frac{m_{C/CMC}}{\rho_{C/CMC}} \tag{S32}$$

where V_i, m_i and ρ_i are the volume, mass and density of *i* before the volume expansion, respectively. The additional superscript "*0*" indicates the state before volume expansion. Obviously, and $0 \le \varphi < \frac{4}{3}\pi R_0^3 / m_{electrode,0}$. Assume C and CMC have a similar density of $\rho_{C/CMC}$. Define the mass ratios of C/CMC to Sn and C to CMC as λ_1 and λ_2, respectively. Namely, $m_{C/CMC} = \lambda_1 m_{Sn}$ and $m_C = \lambda_2 m_{CMC}$. Note that $m_{electrode} = m_{C/CMC} + m_{Sn}$. Consequently,

$$\frac{4}{3}\pi R_0^3 = (1+\lambda_1)m_{Sn}\,\varphi + \frac{m_{Sn}}{\rho_{Sn}} + \frac{\lambda_1 m_{Sn}}{\rho_{C/CMC}} = m_{Sn}[(1+\lambda_1)\varphi + \frac{1}{\rho_{Sn}} + \frac{\lambda_1}{\rho_{C/CMC}}] \tag{S33}$$

In addition,

$$V_{SEI,0} = \frac{4}{3}\pi(R_0+t_0)^3 - \frac{4}{3}\pi R_0^3 \tag{S34}$$

Since the thicknesses of SEI (average: 29.0 and 8.0 nm via cryo-EM) are much smaller than the radii of the micro-sized $Sn/Na_{15}Sn_4$ particles,

$$V_{SEI,0} \approx 4\pi R_0^2 t_0 \tag{S35}$$

After the volume expansion,

$$V_{SEI,d} \approx 4\pi R_d^2 t_d \tag{S36}$$

The constant volume assumption leads to

$$\frac{t_d}{t_0} = \frac{R_0^2}{R_d^2} \tag{S37}$$

After the discharge, the void space may accommodate for some volume expansion. Set the void space utilization ratio as η, and the volume expansion of the sodiated phase (Na_xSn) as ξ. Define the maximal volume expansion as ξ_{max}. Suppose the utilization of the void space is linearly correlated with the volume expansion of the sodiated phase (Na_xSn). Thus,

$$\frac{4}{3}\pi R_d^3 = V_{void,d} + V_{electrode,d} = m_{electrode,0}\varphi\left(1 - \eta\frac{\xi}{\xi_{max}}\right) + V_{Na_xSn} + V_{C/CMC} \tag{S38}$$

$$V_{Na_xSn} = V_{Sn}(1 + \xi) \tag{S39}$$

Assume that the volume of CMC remains constant and the volume of carbon linearly expands with ξ up to ξ_C during the sodiation, and it leads to

$$\frac{4}{3}\pi R_d^3$$

$$= (1 + \lambda_1)m_{Sn}\,\varphi\left(1 - \eta\frac{\xi}{\xi_{max}}\right) + \frac{m_{Sn}}{\rho_{Sn}}(1 + \xi) + \frac{\lambda_1\lambda_2 m_{Sn}}{(1 + \lambda_2)\rho_{C/CMC}}(1 + \xi_C\frac{\xi}{\xi_{max}}) + \frac{\lambda_1 m_{Sn}}{(1 + \lambda_2)\rho_{C/CMC}} = m_{S}$$

$$\lambda_1)\left(1 - \eta\frac{\xi}{\xi_{max}}\right)\varphi + (\frac{1}{\rho_{Sn}} + \frac{\lambda_1\lambda_2}{(1 + \lambda_2)\rho_{C/CMC}}\frac{\xi_C}{\xi_{max}})\xi + (\frac{1}{\rho_{Sn}} + \frac{\lambda_1\lambda_2}{(1 + \lambda_2)\rho_{C/CMC}} + \frac{\lambda_1}{(1 + \lambda_2)\rho_{C/CMC}})] \tag{S40}$$

Thus,

$$\frac{t_d}{t_0}$$

$$= (\frac{R_0^3}{R_d^3})^{\frac{2}{3}} = [\frac{m_{Sn}\left[(1 + \lambda_1)\varphi + \frac{1}{\rho_{Sn}} + \frac{\lambda_1}{\rho_{C/CMC}}\right]}{m_{Sn}\left[(1 + \lambda_1)\left(1 - \eta\frac{\xi}{\xi_{max}}\right)\varphi + \left(\frac{1}{\rho_{Sn}} + \frac{\lambda_1\lambda_2}{(1 + \lambda_2)\rho_{C/CMC}}\frac{\xi_C}{\xi_{max}}\right)\xi + \left(\frac{1}{\rho_{Sn}} + \frac{\lambda_1\lambda_2}{(1 + \lambda_2)\rho_{C/CMC}} + (1\right.\right.}$$

$$=$$

$$\left[\frac{(1 + \lambda_1)\varphi + \frac{1}{\rho_{Sn}} + \frac{\lambda_1}{\rho_{C/CMC}}}{(1 + \lambda_1)\left(1 - \eta\frac{\xi}{\xi_{max}}\right)\varphi + (\frac{1}{\rho_{Sn}} + \frac{\lambda_1\lambda_2}{(1 + \lambda_2)\rho_{C/CMC}}\frac{\xi_C}{\xi_{max}})\xi + (\frac{1}{\rho_{Sn}} + \frac{\lambda_1\lambda_2}{(1 + \lambda_2)\rho_{C/CMC}} + \frac{\lambda_1}{(1 + \lambda_2)\rho_{C/CMC}})}\right]^{\frac{2}{3}} \tag{S41}$$

The normal strain of the SEI, ε, upon the volume expansion is

$$\varepsilon = \frac{\Delta t}{t_0} = \frac{t_d - t_0}{t_0} = \frac{t_d}{t_0} - 1 = \left[\frac{(1+\lambda_1)\varphi + \frac{1}{\rho_{Sn}} + \frac{\lambda_1}{\rho_{C/CMC}}}{(1+\lambda_1)\left(1 - \eta\frac{\xi}{\xi_{max}}\right)\varphi + (\frac{1}{\rho_{Sn}} + \frac{\lambda_1\lambda_2}{(1+\lambda_2)\rho_{C/CMC}}\frac{\xi_C}{\xi_{max}})\xi + (\frac{1}{\rho_{Sn}} + \frac{\lambda_1\lambda}{(1+\lambda_2)}} \right. - 1$$

(S42)

Recall that the volume expansion (ξ) is a function of x in Na_xSn, and the two-phase transition takes place during the sodiation.[S11] The function, defined as $\xi(x)$, is shown in Fig. S23.

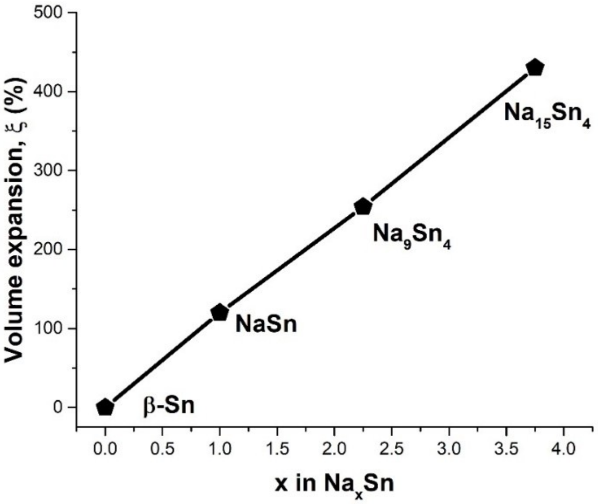

Fig. S23 The volume expansion, $\xi(x)$, of the sodiated phase as a function of sodiation number, x.

Consequently,

$$\varepsilon = \left[\frac{(1+\lambda_1)\varphi + \frac{1}{\rho_{Sn}} + \frac{\lambda_1}{\rho_{C/CMC}}}{(1+\lambda_1)\left(1 - \eta\frac{\xi(x)}{\xi_{max}}\right)\varphi + (\frac{1}{\rho_{Sn}} + \frac{\lambda_1\lambda_2}{(1+\lambda_2)\rho_{C/CMC}}\frac{\xi_C}{\xi_{max}})\xi(x) + (\frac{1}{\rho_{Sn}} + \frac{\lambda_1\lambda_2}{(1+\lambda_2)\rho_{C/CMC}} + \frac{\lambda_1}{(1+\lambda_2)\rho_{C}}} \right.$$

(S43)

The constants in this work are shown as follows. $\lambda_1 = \frac{3}{7}$, $\lambda_2 = 2$, $\rho_{Sn} = 7.3$ g cm^{-3} (β phase), $\xi_{max} = 4.3$, $\xi_{C,diglyme} = 3.47$,[S12] $\xi_{C,EC/DMC} = 0$ (since there is no sodium intercalations into carbon, the volume expansion was assumed to be zero though the other ion storage behaviors such as pore filling may cause expansion) and assume $\rho_{C/CMC} = \rho_C = \rho_{graphite} = 2.3$ g cm^{-3}. The strain of SEI depends on three variables: (i) The sodiation depth, namely, x in Na_xSn; (ii) the void space within the electrodes, φ; (iii) The space utilization ratio, η. Among them, the space utilization ratio, η, depends on the volume expansion homogeneity and the distribution of pores, etc. It is hard to be quantified by available techniques. The void space, φ, can be measured by the porosimetry to be 0.04 cm^3 g^{-1} as shown in Fig. S24.

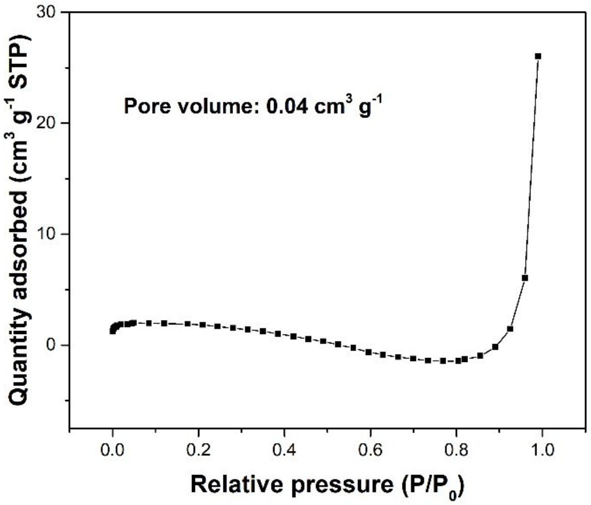

Fig. S24 Nitrogen adsorption/desorption isotherms of Sn microparticle electrode.

Fig. S25 shows some results arising from this model. A few conclusions are drawn from them: (i) The higher space utilization ratio alleviates the strain applied on the SEIs (Fig. S25a,b); (ii) Due to the different volume expansion of carbons in EC/DMC and diglyme, the maximal strains to achieve the theoretical capacity are ~-0.5 and ~-0.6 for the EC/DMC- and diglyme-derived SEIs, respectively; (iii) The higher void space significantly reduces the SEI strain (Fig. S25c,d), which means that nanostructure with sufficient pore volume does help. In comparison to the experimental results, the relative elastic region (~29%) of EC/DMC-derived SEI affords a relatively low capacity (x = 0.67-2.28) if only the reversible elastic deformation happens (Fig. S25a). On the contrary, diglyme-derived SEI is highly tolerant to the volume expansion (~79% versus 60% in Fig. S25b).

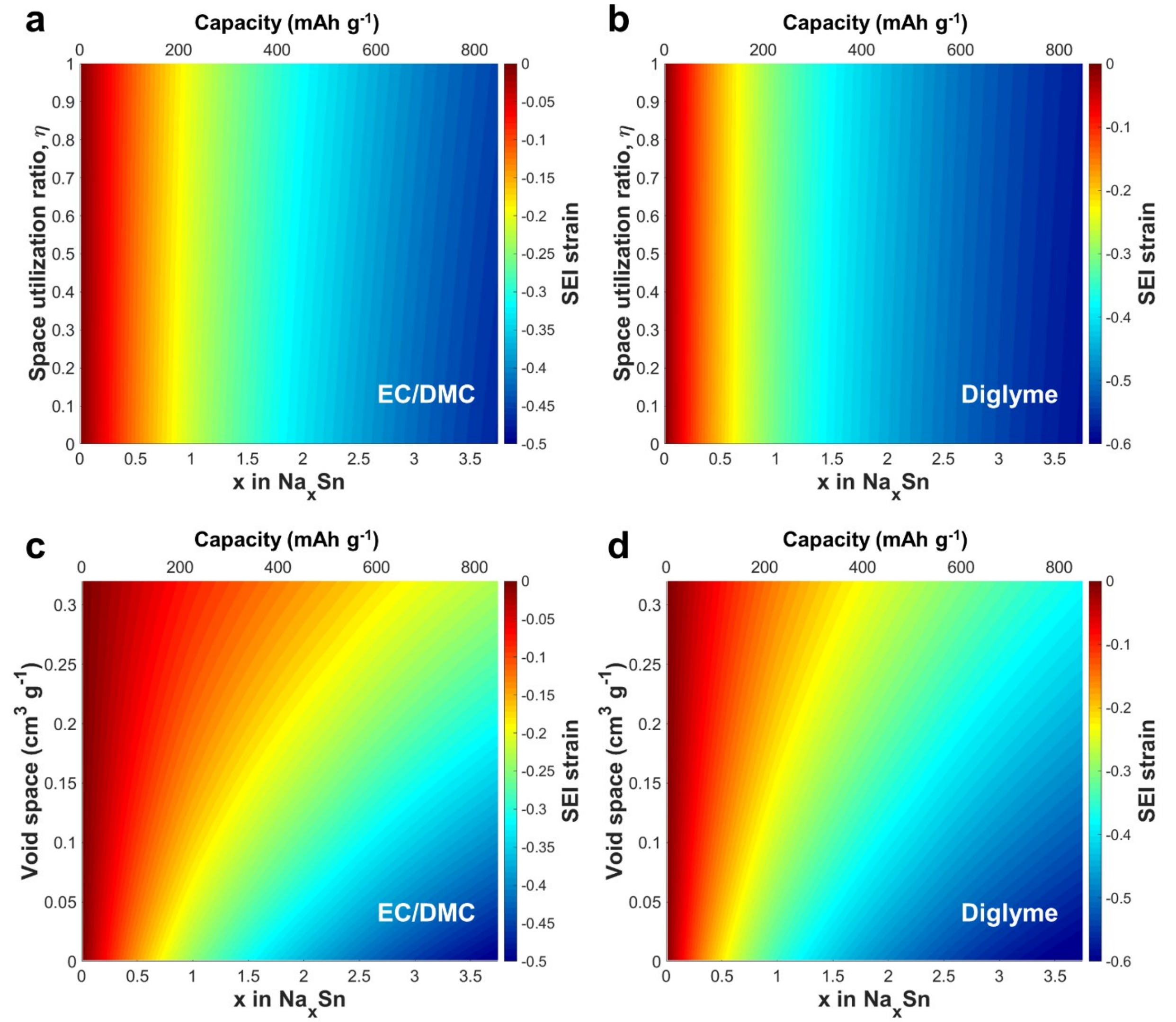

Fig. S25 (a,b)The SEI strain, ε, as a function of x in Na_xSn and space utilization ratio (η), when $\varphi = 0.04$ cm^3 g^{-1} in (a) EC/DMC and (b) diglyme electrolytes. (c,d)The SEI strain, ε, as a function of x in Na_xSn and void space (φ) when $\eta = 0.5$ and $\varphi \leq 0.32$ cm^3 g^{-1} in (c) EC/DMC and (d) diglyme electrolytes.

EIS spectra

The impedance responses at different frequencies characterize the local resistance arising from the different parts of electrochemical cell (Fig. S26),[S13] including (i) R_0, usually the intercept with the real axis, at the high frequency corresponds to the ionic transport resistance of the electrolyte and the electrical resistance from sodium and Sn microparticle electrode; (ii) R_{SEI} at high frequency is correlated with the resistance of the surface films of the Sn microparticle electrode, namely, the SEIs; (iii) R_{ct} at medium frequency indicates the resistance between the SEI and the bulk particles; (iv) the Warburg element at low frequency suggests the sodium diffusion through the Sn bulk material.

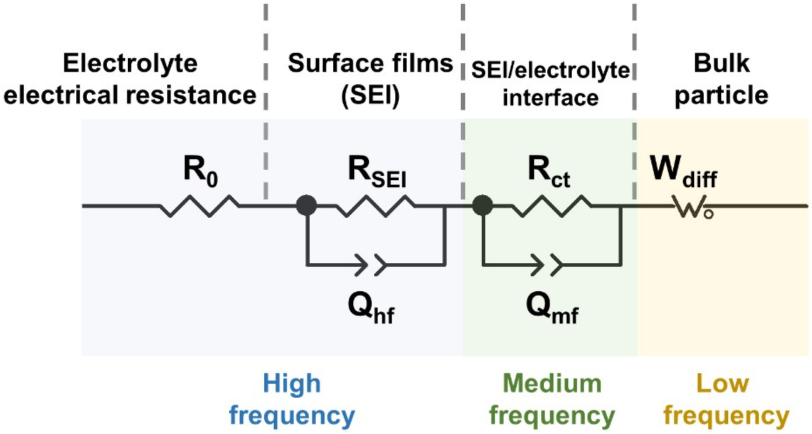

Fig. S26 The equivalent circuit for the EIS fitting.

GITT results

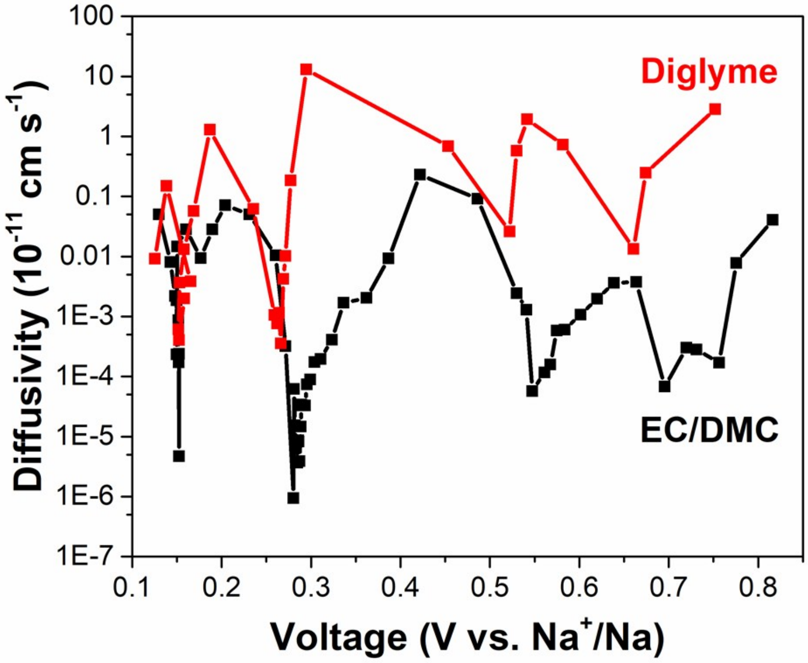

Fig. S27 The apparent diffusivity of sodium ion through Sn microparticle electrodes in $NaBF_4$/diglyme (red) and $NaBF_4$/EC/DMC (black) electrolytes during the charging process. Note that certain peak shifts are seen, due to the larger polarizations in EC/DMC (Fig. 1). In addition, the discharge mostly takes place at a narrow voltage region (<0.2 V vs. Na^+/Na, Fig. 1) and is puzzled by the continuous new SEI formation in EC/DMC (Fig. 1b). Thus, the results of the charge are adopted here.

References

S1. A. Sharma, K. Das, H.-J. Fecht and S. Das, *Appl. Surf. Sci.*, 2014, **314**, 516-522.
S2. K. Kubota and S. Komaba, *J. Electrochem. Soc.*, 2015, **162**, A2538-A2550.
S3. P. E. Blöchl, *Phys. Rev. B: Condens. Matter Mater. Phys.*, 1994, **50**, 17953.
S4. G. Kresse and J. Furthmüller, *Phys. Rev. B: Condens. Matter Mater. Phys.*, 1996, **54**, 11169.
S5. J. P. Perdew, K. Burke and M. Ernzerhof, *Phys. Rev. Lett.*, 1996, **77**, 3865.
S6. S. Grimme, *J. Comput. Chem.*, 2006, **27**, 1787-1799.
S7. D. Aurbach, *J. Power Sources*, 2000, **89**, 206-218.
S8. K. Xu, *Chem. Rev.*, 2004, **104**, 4303-4418.
S9. K. Kanamura, H. Tamura and Z.-i. Takehara, *J. Electroanal. Chem.*, 1992, **333**, 127-142.
S10. J. Zhang, R. Wang, X. Yang, W. Lu, X. Wu, X. Wang, H. Li and L. Chen, *Nano Lett.*, 2012, **12**, 2153-2157.
S11. B. Zhang, G. Rousse, D. Foix, R. Dugas, D. A. Corte and J. M. Tarascon, *Adv. Mater.*, 2016, **28**, 9824-9830.
S12. H. Kim, J. Hong, G. Yoon, H. Kim, K.-Y. Park, M.-S. Park, W.-S. Yoon and K. Kang, *Energy Environ. Sci.*, 2015, **8**, 2963-2969.
S13. M. Levi, G. Salitra, B. Markovsky, H. Teller, D. Aurbach, U. Heider and L. Heider, *J. Electrochem. Soc.*, 1999, **146**, 1279-1289.